

Probing Mg Migration in Spinel Oxides

Ryan D. Bayliss,^{†,‡,§,¶,||} Baris Key,^{‡,||,††,ID} Gopalakrishnan Sai Gautam,^{‡,§,¶,||} Pieremanuele Canepa,^{‡,§,¶,||}
 Bob Jin Kwon,^{†,||} Saul H. Lapidus,^{‡,¶,||} Fulya Dogan,^{||,ID} Abdullah A. Adil,[†] Andrew S. Lipton,^O
 Peter J. Baker,^{♦,ID} Gerbrand Ceder,^{‡,§,¶,||} John T. Vaughan,^{‡,||,ID} and Jordi Cabana^{*,†,‡,ID}

[†]Department of Chemistry, University of Illinois at Chicago, Chicago, Illinois 60607, United States

[‡]Joint Center for Energy Storage Research, ^{||}Chemical Sciences and Engineering, and [▽]Advanced Photon Source, X-ray Science Division, Argonne National Laboratory, Lemont, Illinois 60439, United States

[§]Department of Materials, University of Oxford, Oxford OX2 6HT, U.K.

¹Department of Materials Science and Engineering, Massachusetts Institute of Technology, Cambridge, Massachusetts 02139, United States

[#]Materials Science Division, Lawrence Berkeley National Laboratory, Berkeley, California 94720, United States

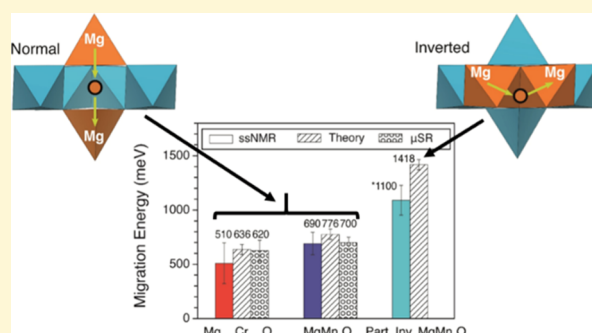
[¶]Department of Materials Science and Engineering, University of California, Berkeley, Berkeley, California 94720, United States

^oEnvironmental Molecular Sciences Laboratory, Pacific Northwest National Laboratory, Richland, Washington 99354, United States

[♦]ISIS Pulsed Neutron and Muon Source, Rutherford Appleton Laboratory, Didcot OX11 0QX, UK

S Supporting Information

ABSTRACT: Mg batteries utilizing oxide cathodes can theoretically surpass the energy density of current Li-ion technologies. The absence of functional devices so far has been ascribed to impeded Mg^{2+} migration within oxides, which severely handicaps intercalation reactions at the cathode. Broadly, knowledge of divalent cation migration in solid frameworks is surprisingly deficient. Here, we present a combined experimental and theoretical study of Mg migration within three spinel oxides, which reveal critical features that influence it. Experimental activation energies for a Mg^{2+} hop to an adjacent vacancy, as low as ~ 0.6 eV, are reported. These barriers are low enough to support functional electrodes based on the intercalation of Mg^{2+} . Subsequent electrochemical experiments demonstrate that significant demagnesiation is indeed possible, but the challenges instead lie with the chemical stability of the oxidized states. Our findings enhance the understanding of cation transport in solid structures and renew the prospects of finding materials capable of high density of energy storage.



■ INTRODUCTION

Research of multivalent batteries has received increased attention following the conceptual demonstration of a Mg battery in 2000.¹ Batteries that pair a metallic Mg anode against a high-voltage intercalation cathode could lead to substantially higher energy density than the current Li-ion technology,² thus advancing applications such as electric vehicles, critical in a shift toward sustainability. Reversible Mg electrodeposition has been demonstrated, albeit in electrolytes with relatively low anodic stability.³ On the cathode side, in contrast, the lack of materials that undergo reversible Mg intercalation remains the major hurdle toward a practical battery.⁴ Although it has been demonstrated in sulfides such as MgMo_6S_8 and MgTi_2S_4 ,^{1,5} both the associated specific capacities and voltages of operation are too low to produce devices with competitive energy densities. Both can potentially be raised if oxides are employed instead.⁴

Oxides with a spinel structure are predicted to provide a favorable combination of capacity, voltage of operation, and ionic mobility, which underpin the metrics of a cathode. Although preliminary evidence of reversible intercalation into $\lambda\text{-Mn}_2\text{O}_4$ exists,⁶ it also clearly revealed that the electrochemical reaction presented significant inefficiencies, likely kinetic, relative to analogous reactions with Li. Generally, the lack of solid oxides capable of extensive and reversible Mg intercalation is ascribed to low cation mobility because of strong Coulombic repulsions during the Mg^{2+} cation hop between sites. However, no experimental evaluation of the barriers for Mg^{2+} migration in oxides is available. The performance of Mg cathodes under electrochemical conditions

Received: June 23, 2019

Revised: December 18, 2019

Published: December 19, 2019

is highly susceptible to cation desolvation, solvent cointercalation,⁷ and conversion reactions,⁴ highlighting the importance of directly measuring bulk Mg phenomena. These measurements also provide valuable means to “close the loop” with existing theoretical predictions and eventual cathode design.

Contrary to existing assumptions, here, we demonstrate that the barriers of Mg^{2+} migration in spinel oxides with Cr and Mn are sufficiently low to support electrode function at reasonable particle sizes. A combination of powder diffraction, ²⁵Mg variable temperature solid-state nuclear magnetic resonance (VT ss-NMR), and muon spin relaxation (μ SR) studies reveals Mg hoping barriers of \sim 600 meV, in excellent agreement with independent density functional theory (DFT) predictions. Thus, our findings challenge the existing notion that cation migration in oxides is the primary limiting factor hindering the development of functional Mg cathodes. Indeed, the possibility of electrochemically deintercalating Mg^{2+} is demonstrated for normal spinels. Our results also indicate that Mg ion migration is notably sensitive to structural disorder within the spinel lattice, which can be controlled during the synthesis. This work provides renewed motivation toward developing high-voltage Mg batteries.

■ EXPERIMENTAL SECTION

Synthesis of Metal Oxides. The synthesis of samples was performed through either a sol–gel-type synthetic route or a ceramic high-temperature synthesis. For the sol–gel route, the desired metal acetates were added in stoichiometric ratios to 100 mL of deionized water. The total concentration of ions in solution was 0.025 mol. A further 0.025 mol of citric acid was added to the solution at a 1:1 ratio with the total metal ion concentration. The solution was stirred on a hot plate in a fume hood just below the boiling point until all the water had evaporated. The remaining sol was then placed in a box furnace inside a fume hood and heated to 450 °C for 6 h, ramping at 10 °C/min. The resultant black foam was then ground in a mortar and pestle to a fine powder. The sample was transferred to a ceramic high-alumina crucible and heated to 1000 °C for 12 h in air, ramping at 10 °C/min. For the $MgMn_2O_4$ samples, the resultant powder was then split into two parts for subsequent thermal annealing to obtain various extents of inversion in the spinel. To obtain a normal spinel, the sample was placed in a box furnace in air at 400 °C for 100 h and quenched in liquid N₂. To obtain the partially inverted spinel, the sample was placed in a box furnace in air at 1000 °C for 60 h and quenched in liquid N₂. For the ceramic high-temperature synthesis, magnesium hydroxide and chromium nitrate nonahydrate were mixed together in stoichiometric ratios, heated to 250 °C for 2 h, and then heated to 1000 °C for 16 h.

Electrochemical Experiments. Powders were mixed with acetylene black with a 60/40 mass ratio and drop-cast onto 1.5" stainless steel current collectors (25–35 mg of active material). The electrodes were introduced into Swagelok-type stainless steel cells with a Li metal counter electrode and 1.0 M LiPF₆ in a 3:7 (wt %/wt %) mixture of ethylene carbonate and ethyl methyl carbonate. Experiments were conducted at 50 °C, and for constant current experiments, a C/20 rate was used. Samples were handled in inert Ar atmosphere except when sample sensitivity to X-rays and air were tested. Electrochemical samples were additionally characterized by lab X-ray diffraction (XRD) using Cu K α radiation (Bruker D8) and transmission electron microscopy (TEM) with an energy-dispersive X-ray detector (JEOL JEM 3010) operated at 300 kV.

Synchrotron XRD (APS, 11-BM-B). Samples were loaded in Kapton capillaries (0.9 mm diameter) and mounted on bases provided by the Advanced Photon Source (APS), Argonne National Laboratory. High-resolution synchrotron powder diffraction data were collected using beamline 11-BM-B with an average wavelength of 0.414 Å for all compounds. Two platinum-striped collimating mirrors and a double-crystal Si(111) monochromator are used for the X-ray

optics.⁸ The data points were collected at room temperature with a step size of 0.001° 2θ and a scan speed of 0.01°/s. Data are collected while continually scanning the diffractometer 2θ arm. High resolution and short collection time are obtained by using a unique 12-element Si(111) crystal analyzer/detector.⁹ Rietveld refinements¹⁰ were performed using TOPAS version 4.1 by Bruker AXS (version 4.1, 2008). All diffraction plots are presented in Q (Å⁻¹), where $Q = [4\pi \sin(\theta)]/\lambda$.

Time-of-Flight Neutron Powder Diffraction (NOMAD, BL-1B, and Spallation Neutron Source). Time-of-flight (ToF) total scattering neutron data were collected on the nanoscale-ordered materials diffractometer (NOMAD), the spallation neutron source, Oak Ridge National Laboratory, which has a total flight path of 21.5 m and utilizes a neutron beam collimated down to a diameter of \sim 6 mm.¹¹ Samples were preloaded 2 cm high in 3 mm diameter quartz glass capillaries available from Hampton Research, CA, USA, and sealed with an epoxy resin. NOMAD detectors were calibrated using scattering from diamond powder, and the instrument parameter file for the Rietveld refinements was obtained from the measurements of the NIST standard silicon powder. All diffraction plots are presented in Q (Å⁻¹).

ss-NMR Spectroscopy. ²⁵Mg magic angle spinning (MAS) NMR experiments were performed at 11.7 T (500 MHz) on a Bruker ADVANCE III spectrometer operating at a Larmor frequency of 30.64 MHz using a 3.2 mm MAS probe and at 19.89 T (850 MHz) on a Varian Direct Drive (VNMR) spectrometer operating at a Larmor frequency of 52.22 MHz using a 4 mm MAS probe. A calibrated $\pi/2$ (actual $\pi/6$) pulse width of 3 μ s was used with sufficiently long pulse recycle delays of 0.2–0.5 s. The spectra were acquired at a spinning speed of 20 kHz for 3.2 mm rotors (10 and 15 kHz for 4 mm rotors) with a rotor-synchronized spin echo experiment ($90^\circ - \tau - 180^\circ - \tau$), where τ is $1/\nu_r$. For high-field measurements, a calibrated $\pi/2$ (actual $\pi/6$) pulse width of 2 μ s was used with pulse recycle delays of 0.2 s and spinning speeds of 10 kHz again with rotor-synchronized spin echo experiments. To ensure quantification in normalized intensity experiments, single-pulse experiments (data not shown) with recycle delays 0.1–1 s were used to confirm signal saturation. All chemical shifts were referenced to 5 M MgCl₂ (aq) at 0 ppm. Quadrupolar fits to the spectra were constrained to Lorentzian-only with seven sidebands for Cr-spinel and three sidebands for normal Mn-spinel. The fits produced overlaps >80%, had $\pm 5\%$ error in quadrupolar coupling constants and full width at half-maximum (fwhm), and had negligible error in shifts.

Muon Spin Relaxation. Muon measurements were carried out using the EMU spectrometer at the STFC ISIS pulsed neutron and muon source on unenriched samples of normal and partially inverted $MgMn_2O_4$ and $MgCr_2O_4$.¹² Spin-polarized positive muons are implanted within the material where they stop rapidly at interstitial sites without loss of spin polarization.¹³ The implanted muon spins are sensitive to static and dynamic magnetic fields within the sample. After implantation, the polarization of the muon ensemble evolves with time and is recorded using the decay of muons into positrons, which is asymmetric with respect to the muon spin direction at the instant of decay. The experiment on the normal spinel $MgMn_2O_4$ was carried out similarly to those previously demonstrated in studying lithium battery materials.¹⁴ Measurements were made at a series of temperatures and small magnetic fields applied along the direction of the initial muon spin polarization. The data were analyzed using a dynamic Gaussian Kubo Toyabe function,¹⁵ multiplied by an exponential relaxation, to extract for each temperature a static field distribution width Δ resulting from nuclear moments, a fluctuation rate ν from nuclear moments moving past the muon, and a damping rate λ due to electronic (paramagnetic) fluctuations.

First-Principles Calculations of Hopping Barriers. Mg hopping barriers were computed using the nudged elastic band (NEB) method together with DFT,^{16,17} as implemented in the Vienna Ab initio Simulation Package (VASP).^{18,19} The Perdew–Burke–Ernzerhof implementation of the generalized gradient approximation functional is used to describe the exchange–correlation interactions.²⁰ Fictitious interactions across periodic images are minimized by

introducing a minimum distance of at least 8.6 Å between the Mg ions and eight or nine distinct images are used between the end points to capture the diffusion trajectory. The end point energies of the spinel structures were converged to 0.01 meV/supercell, while the forces in the NEB are considered converged within 0.05 eV/Å.

RESULTS AND DISCUSSION

Spinel-type AB_2X_4 oxides crystallize in a cubic close-packed oxygen lattice. In a normal framework, 1/8 of the tetrahedral and 1/2 of the octahedral sites are occupied by A and B cations, respectively. Disordered, or inverted, configurations can arise depending on several competing factors, including the crystal field stabilization energies of the transition metals (B cations) and entropic considerations.²¹ In this study, two initially identical samples of $MgMn_2O_4$ were rapidly quenched after annealing at 400 and 1000 °C, respectively.²² Combined synchrotron X-ray (XRD) and ToF neutron powder diffraction (ToF-NPD) revealed that both samples crystallized in single-phase tetragonal lattices (space group $I4_1/AMD$, Figure 1), in

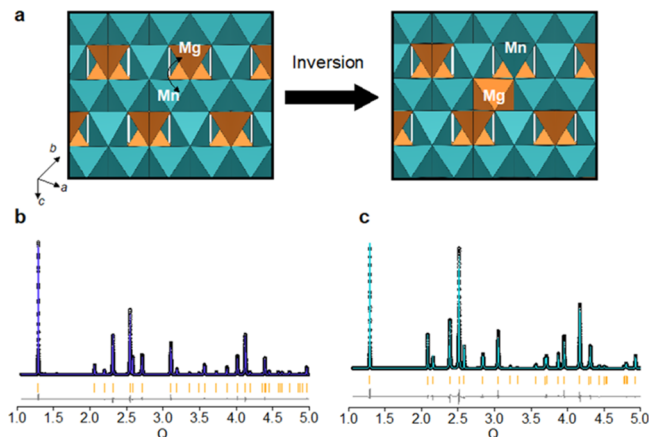


Figure 1. (a) Schematic showing the local coordination of Mg in normal and inverted spinels and final Rietveld refinements of (b) normal ($(Mg)[Mn_2]O_4$) and (c) partially inverted ($(Mn_{0.41}Mg_{0.59})[Mn_{1.59}Mg_{0.41}]O_4$) spinels.

agreement with the presence of Jahn–Teller active Mn^{3+} ions. Combined Rietveld refinements revealed structures of $(Mg)[Mn_2]O_4$ (Figures 1b, S1, and S2 and Table S1) and $(Mg_{0.59}Mn_{0.41})[Mg_{0.41}Mn_{1.59}]O_4$ (Figures 1c, S3, and S4 and Table S2) for the samples quenched from 400 to 1000 °C, respectively, where () and [] denote the occupancy of tetrahedral and octahedral sites, respectively. Expectedly, in appropriate conditions, a fraction of Mg^{2+} in $(Mg)[Mn_2]O_4$ can exchange with Mn^{3+} , giving rise to partially inverted lattices (Figure 1a), accompanied by charge disproportionation ($2Mn^{3+} \rightarrow Mn^{2+} + Mn^{4+}$).²³ Investigation of the local environment via neutron pair distribution function (PDF) suggested that the local bond lengths are significantly more varied in partially inverted $(Mg_{0.59}Mn_{0.41})[Mg_{0.41}Mn_{1.59}]O_4$ compared to the normal structure $(Mg)[Mn_2]O_4$ (Figures S5 and S6). Variation of the local Mg environments within a framework can have significant implications for local migration.²⁴ To assess the effect of transition metal on Mg migration, a magnesium chromium oxide was also prepared. Rietveld refinement revealed a normal spinel framework, with a cubic $F\bar{d}\bar{3}m$ lattice (Figure S7 and Table S3). The ordered arrangement is driven by the crystal field stabilization energy for Cr^{3+} , with a d^3 electronic configuration, which strongly

favors octahedral coordination.²¹ Refinements also concluded a slightly off-stoichiometric final composition $(Mg)[Mg_{0.15}Cr_{1.85}]O_4$ (average valence, $Cr^{3.08+}$) and a minor amount of Cr_2O_3 (~8 wt %).

^{25}Mg ss-NMR spectroscopy probed the local Mg environment (Figures 2 and S8). A sharp, single isotropic resonance at

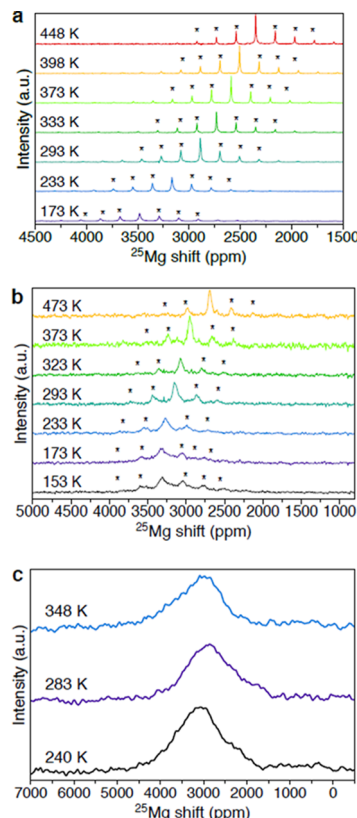


Figure 2. VT ^{25}Mg MAS NMR of (a) normal spinel ($(Mg)[Mg_{0.15}Cr_{1.85}]O_4$) collected at 19.89 T, (b) normal ($(Mg)[Mn_2]O_4$) collected at 19.89 T, and (c) partially inverted spinel ($(Mn_{0.41}Mg_{0.59})[Mn_{1.59}Mg_{0.41}]O_4$) collected at 11.7 T. * indicates spinning sidebands.

~2809 ppm was observed in the spectrum of $(Mg)[Mg_{0.15}Cr_{1.85}]O_4$ at 293 K (Figure 2a), originating from Fermi contacts between Mg and transition metals in the local coordination shell.²⁵ The sharp and intense signal is ascribed to Mg occupying highly symmetrical tetrahedral sites. Excess Mg in $(Mg)[Mg_{0.15}Cr_{1.85}]O_4$ is likely to be statically distributed across the octahedral sites (Mg'_{Cr}), which was, based on the crystal structure analysis from XRD, assigned to a small broad peak at ~2715 ppm at 333 K (Figure S9). The remaining peaks in the spectrum are sidebands resulting from the partial averaging of dipolar couplings by spinning the sample during the measurement.

In the case of normal $(Mg)[Mn_2]O_4$ (Figure 2b), a single sharp resonance was observed at ~3075 ppm at 293 K, as recently reported.²⁶ In contrast to both normal spinel structures ($(Mg)[Mn_2]O_4$ and $(Mg)[Mg_{0.15}Cr_{1.85}]O_4$), a very broad peak centered at ~2900 ppm was found in the ^{25}Mg NMR spectrum of the inverted $(Mg_{0.59}Mn_{0.41})[Mg_{0.41}Mn_{1.59}]O_4$ at 283 K (Figure 2c). The broad signal can be ascribed to a statistical distribution of Mg^{2+} in both tetrahedral and octahedral sites, coupled with the presence of a variety of Mn–O–Mg environments with Mn assuming different oxidation states (i.e., +2, +3, and +4), as a result of inversion.

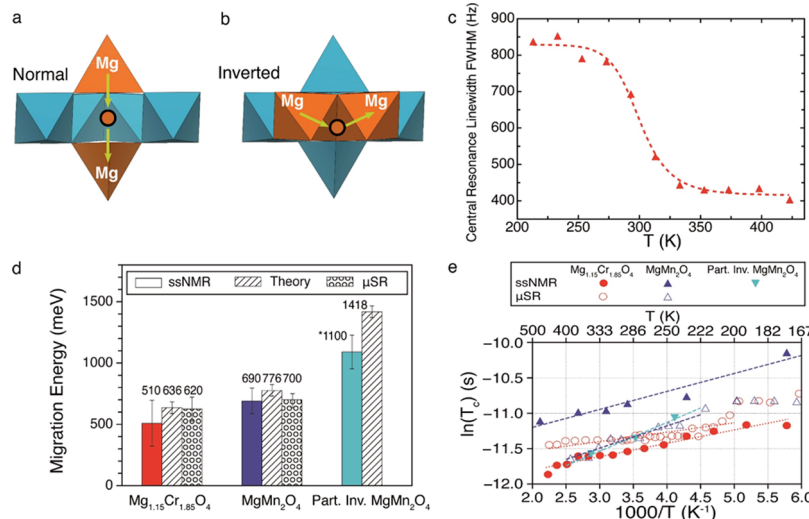


Figure 3. (a,b) Local cation arrangement in normal and inverted spinels, with arrows highlighting the local order effects on Mg migration pathways. (c) Temperature-dependent NMR peak width change regimes for VT ^{25}Mg MAS NMR resonance of $(\text{Mg})[\text{Mg}_{0.15}\text{Cr}_{1.85}]\text{O}_4$. (d) Experimentally and theoretically calculated activation energies for ion migration in the three spinels. * indicates a semiquantitative estimate due to poor spectral resolution. (e) Correlation times τ_c , derived from VT ^{25}Mg MAS NMR and μSR , in spinel oxides with Mn (violet and cyan dashed lines) and Cr (red dotted line). The NMR data were collected on $(\text{Mg})[\text{Mg}_{0.15}\text{Cr}_{1.85}]\text{O}_4$ made by a solid-state method, whereas μSR was collected on MgCr_2O_4 made by sol–gel.

This result is in good agreement with both the long-range averaged Rietveld refinement and the local bonding environment variations qualitatively observed via neutron PDF.

The possibility of probing local Mg migration was also examined via NMR, based on an established track record of showing agreement with macroscopic measurements of ionic conductivity.^{27,28} The presence of largely single resonances in the ^{25}Mg NMR response eliminated the use of 2D methods,²⁹ whereas the presence of paramagnetic ions and the nuclear properties of ^{25}Mg made the utilization of relaxometry³⁰ challenging and precluded pulse field gradient techniques,³¹ respectively. However, semiquantitative measurements of local dynamics could be possible within the NMR time scales using data at variable temperature when line shapes are well defined (Figure 2a,b, with complete series in Figures S10 and S11),^{32,33} especially when strong homonuclear coupling is absent (10% natural abundance of ^{25}Mg) and structural knowledge of the Mg environment exists. Fermi contact resonances, particularly for highly quadrupolar nuclei such as ^{25}Mg ,³⁴ are typically broad because of the large dipolar coupling with unpaired electrons in the transition metals but can be averaged by fast ion motion in the coordination environment. Therefore, the rather sharp character of the ^{25}Mg NMR signal ($\text{fwhm} < 2.5$ kHz) in the two normal spinels suggest contributions originating from local motion of Mg^{2+} , in analogy with related Li-ion battery materials.³⁵ In a normal spinel (Figure 3a), such motion can be modeled through hops between tetrahedral sites (8a) via vacant (intermediate) octahedral sites (16c). Significant narrowing of the NMR peaks was observed going from 153 to 473 K (Figure 2a,b). Peak narrowing takes place when the rate of fluctuations of the local magnetic and/or electric fields around the probed nucleus is higher than the NMR time scale (further detailed in Supporting Information). Motion of Mg^{2+} within the lattice could induce such rapid fluctuations of the local environment, resulting in an NMR signal that represents a time average of all the configurations during a cation hop. The Fermi contact shift varied strongly as a function of temperature, reflecting its dependence on

magnetic susceptibility, which decreases with temperature.^{25,35} In contrast to the normal spinels, the partially inverted $(\text{Mg}_{0.59}\text{Mn}_{0.41})[\text{Mg}_{0.41}\text{Mn}_{1.59}]\text{O}_4$ (Figure 2c) showed minimal peak narrowing as the temperature increased, indicative of negligible ionic motion. In this case, because Mg^{2+} ions also partly occupy octahedral transition-metal sites (16d), they must move through vacant (intermediate) tetrahedral sites (48f) (Figure 3b). The fact that $(\text{Mg}_{0.59}\text{Mn}_{0.41})[\text{Mg}_{0.41}\text{Mn}_{1.59}]\text{O}_4$ shows negligible dynamics while having the highest electronic conductivity, associated with the concurrently highest concentration of transition metals in mixed oxidation states,²² indicates that these motional processes are not driven by electron hopping.

Fits of the normal spinel spectra (Figures S12–S16) revealed small quadrupolar couplings and temperature-dependent asymmetry parameters, which enable the analysis of motional dynamics from the line width of the central resonance.³⁰ In the case of $(\text{Mg})[\text{Mg}_{0.15}\text{Cr}_{1.85}]\text{O}_4$, a transition from a Gaussian to a Lorentzian line shape of the entire spinning sideband manifold accompanied by sharp narrowing was detected with an onset temperature, T_c , of 275 K (Figures 2b, 3c, and S18). Below T_c , the rigid lattice limit operates, where any motion is extremely slow.³⁰ At these conditions, a line width for the central resonance $\delta_0 \approx 800$ Hz could be measured, whereas the width of the signal envelope, including all observable spinning sidebands, was $\delta\omega_0 \approx 25$ kHz, approaching the static line. An approximate empirical activation energy for motional narrowing (E_a^{MN}) was extracted according to the Waugh and Fedin model, $E_a^{\text{MN},\text{WF}} = 1.617 \cdot T_c = 445$ meV.³⁶ Alternatively, E_a^{MN} can be extracted by fitting δ versus T according to the ad hoc formalism shown in eq 1,^{30,37} where δ_0 and δ_∞ denote the line width below and above the onset temperature, respectively, where ς is a fit parameter here chosen to be 1, k_B denotes Boltzmann's constant, and τ_0^{MN} represents the pre-exponential factor of the corresponding correlation time τ_c^{MN} . This fit, presented as a dashed line in Figure 3c, led to $E_a^{\text{MN}} = 510 \pm 190$ meV for Mg hopping barriers.

$$\delta(T) = \sqrt{\delta_0^2 \frac{2}{\pi} \arctan \left[\zeta \delta(T) \tau_0^{MN} \delta \exp \left(\frac{E_a^{MN}}{k_B T} \right) \right] + \delta_\infty^2} \quad (1)$$

A clear onset in narrowing of the line shape due to paramagnetic broadening was not captured for $(Mg)[Mn_2]O_4$, inhibiting a direct comparison to $(Mg)[Mg_{0.15}Cr_{1.85}]O_4$; however, a similar transition from Gaussian to a Lorentzian line shape for the spinning sideband manifold for the normal spinel accompanied by a more symmetric envelope is observed ~ 293 K, suggesting similar dynamics for the normal spinels. Consequently, cation dynamics were estimated from the trends in line width with temperature (Figure S19), a methodology validated for Li conductors.^{32,33} Motional fluctuations in NMR signals are generally described by a correlation time, τ_c . In the rigid lattice limit (e.g., below 250 K), $1/\tau_c \approx \delta\omega_0$, where, again, $\delta\omega_0$ corresponds to the total width, including sidebands, of the NMR signals at a given temperature. When signal narrowing occurs, the relationship changes, with τ_c being given by the Bloembergen–Purcell–Pound theory,³⁸ via eq 2.

$$(\Delta v)^2 = \left(\frac{2}{\pi} \right) \delta\omega_0^2 \tan^{-1}(\tau_c \Delta v) \quad (2)$$

The corresponding dependence of τ_c with temperature from the NMR spectra followed an Arrhenius-type behavior (Figure 3e), implying that the slopes within the experimental temperature region are inversely correlated with the relative migration rate in the different lattices. However, the presence of paramagnetic centers in the samples can alter the measured activation barriers,³³ potentially resulting in unrealistically low values from a direct fit of $\ln \tau_c$ versus $1/T$. Therefore, this method of analysis was first calibrated against the E_a^{MN} of $(Mg)[Mg_{0.15}Cr_{1.85}]O_4$ experimentally determined above (Figure 3c). A more detailed explanation of this process as well as the assumptions made are available as Supporting Information. Subsequently, we obtained E_a^{MN} of 690 ± 90 and 1100 ± 140 meV for $(Mg)[Mn_2]O_4$ and $(Mg_{0.59}Mn_{0.41})[Mg_{0.41}Mn_{1.59}]O_4$, respectively. It is important to note that NMR artifacts can arise from Mn mixed valency and multiple Mg sites in the inverted spinel, increasing the systematic errors of the analysis. The number obtained for the inverted spinel is significantly lower than the theoretical prediction, which is consistent with the semiquantitative nature of this analysis, induced by both the existence of unquantifiable errors when attempting to establish reliable line widths originating from magnetic and paramagnetic effects, and limitations of BPP theory in probing activation energy. Nonetheless, the large difference in hopping barrier upon inversion demonstrates unambiguously that Mg^{2+} dynamics is significantly impeded by the presence of Mg–Mn antisite defects.

Because of the significant challenges in quantifying parameters of mobility accurately using NMR line width changes, such as complexities of the lattice, and changes in local magnetic and/or electronic structures,^{28,30} the results were further supported by μ SR. μ SR assessed Mg migration in $(Mg)[Mn_2]O_4$, $(Mg_{0.59}Mn_{0.41})[Mg_{0.41}Mn_{1.59}]O_4$, and $MgCr_2O_4$ made by a sol–gel method to avoid interferences from Cr_2O_3 in the $(Mg)[Mg_{0.15}Cr_{1.85}]O_4$ sample. Analogous studies have recently been demonstrated for Li battery electrode materials.^{14,39} In normal $(Mg)[Mn_2]O_4$, the raw signal (Figure S20) was dominated by nuclear magnetic fields with a Gaussian distribution, and temperature-dependent

fluctuations, as observed in lithium dynamics.¹⁴ Fits of the μ SR data were carried at multiple temperatures. The relaxing asymmetry of the muon data (Figure S21) was around half the value that would be expected for a sample of the same size with 100% abundant nuclear moments, which can be attributed to the 10% abundance of ^{25}Mg giving a nuclear field distribution on some but not all sites. With increasing temperature, Δ decreased slightly (Figure S22) and λ remained small and nearly constant (Figure S23). Similar trends were observed with $MgCr_2O_4$ (Figures S24 and S25), but, to ensure consistent fitting, λ was held constant at 0.045 MHz.

At low and high temperatures, the fluctuation rate of μ SR, $v = 1/\tau_c$, was nearly constant, with a sudden increase observed from ~ 250 to 400 K, because of the thermally activated motion of ^{25}Mg nuclei falling within the time range to which muons are sensitive. The corresponding τ_c values are shown in Figure 3e. Fitting an Arrhenius form led to an activation energy, $E_a = 700 \pm 60$ meV for $(Mg)[Mn_2]O_4$, in good agreement with values obtained from NMR. For $MgCr_2O_4$, the higher-temperature behavior suggests $E_a = 620 \pm 100$ meV, with τ_c being very similar to the NMR results at the same temperatures. At lower temperatures, there was more scatter in the μ SR data, but the overall trend was consistent. In contrast, the muon signal of $(Mg_{0.59}Mn_{0.41})[Mg_{0.41}Mn_{1.59}]O_4$ was dominated by larger electronic magnetic fields. The fitting function used for the data from normal spinels was found to give a poor description of the data with poorly constrained parameters. Instead, an excellent description of the data was achieved by fitting to a single exponential relaxation (Figures S26 and S27). This behavior is conventional for a paramagnetic sample with large electronic moments fluctuating strongly, obscuring the nuclear magnetic fields, and precluding assessment of the Mg^{2+} dynamics in this phase. The presence of Mn^{2+} ($\sim 5.9\mu_B$) in the tetrahedral sites alongside $^{25}Mg^{2+}$ ($-0.86\mu_N$, 10% abundance) is likely to underlie this difference, also suggesting that the stopping site of the muons is more sensitive to the A-site behavior.

Further insight of Mg^{2+} migration was obtained from first-principles DFT calculations of trajectories within the high vacancy regime ($x_{Mg} = 0.125$, Figure 3a,b). The hopping barrier in both normal (tet \rightarrow oct \rightarrow tet) and inverted (oct \rightarrow tet \rightarrow oct) spinels is set by the triangular face shared between the stable and intermediate sites, reflecting the typical “valley”-shaped migration energy landscape (Figure S28).⁴⁰ The predicted barrier for a Mg hop in the normal spinel structure is ~ 776 meV for Mn_2O_4 and ~ 636 meV for Cr_2O_4 (Figure 3d), in good agreement with the experimental observations from ^{25}Mg NMR and μ SR (Figure 3d). In the case of inversion, a situation of partial Mg/Mn exchange at $x_{Mg} = 0.25$, that is, $(Mn_{0.25}Mg_{0.125})[Mg_{0.125}Mn_{1.75}]O_4$ (corresponding to a degree of inversion of 0.25), was modeled. In this case, the Mg migration barrier was ~ 1418 meV (Figure 3c), significantly higher than in the normal spinel. The large increase is driven by the electrostatic penalty associated with the close proximity of divalent ions as a result of the edge sharing between the intermediate 48f tetrahedral site and an adjacent tetrahedral 8a site. The value is in good qualitative agreement with NMR measurements (Figure 3d), especially when the trends between phases are considered. The increase in hopping barriers in inverted spinels not only indicates a drastic reduction in Mg^{2+} cation dynamics but is also in agreement with previous theoretical predictions of poor migration in oxide structures with Mg octahedral occupancy.^{40,41} The good general

agreement between theory and experimentally measured activation energies corroborates our approach.

NMR and μ SR indicate that the rate of successful Mg hops at room temperature is $\nu \approx 60$ kHz. Consideration of potential diffusion pathways suggests an atomic jump distance, $a \approx 3$ Å.⁴⁰ The diffusivity can thus be approximated as $D \approx \nu \times a^2 \times \exp(-E_a/k_B T) \approx 5 \times 10^{-11}$ cm²/s at room temperature. Coupled with the existence of many percolating pathways in a normal spinel structure,³⁷ this value would make it possible for a 1 μ m particle to fully (de)magnesiate at acceptable rates. A particle of 100 nm may permit values up to ~ 740 meV based on these assumptions.⁴⁰ It is exciting that this estimated value matches well with both normal oxide spinels. Therefore, while the measured barriers are high compared to those of superionic conductors, they should be sufficient to lead to feasible Mg battery cathodes even when conventionally engineered. With this hypothesis in mind, electrochemical deintercalation of Mg²⁺ was attempted. MgCr₂O₄ was made by a sol–gel method to combine the lowest measured activation energy with the smallest particle size. Because of the lack of functional Mg electrolytes at the potentials predicted for deintercalation (up to 4.2 V vs Mg²⁺/Mg⁰),⁴² experiments were performed galvanostatically at C/20 in a conventional Li metal half-cell. The potential of the cell (Figure 4a) raised rapidly above 4.5 V versus Li⁺/Li⁰ (3.8 V vs Mg²⁺/Mg⁰) and reached around 5 V versus Li⁺/Li⁰ (4.3 V vs Mg²⁺/Mg⁰), where 220 mA h/g could be accumulated.

The ²⁵Mg MAS NMR spectrum of sol–gel MgCr₂O₄ showed the expected sharp signal at ~ 2800 ppm and a minor peak at 2970 ppm because of the small amount of Mg in octahedral sites. In turn, charged samples systematically shifted to lower frequencies, with complex line shapes (Figure 4b), consistent with the decrease in unpaired electrons upon oxidation of Cr⁺³ to Cr⁺⁴ ($3d^3$ to $3d^2$). Slight differences in shift were observed with and without a hold at 5.0 V (2524 vs 2560 ppm). The normalized intensities of these spectra were only 29 and 35% of pristine, indicating removal of 71 and 65% Mg²⁺, respectively. Complementary TEM–energy-dispersive X-ray (EDX) also revealed a significant decrease in the Mg/Cr ratios after a potentiostatic hold (Figure S29). Taken together, these observations are consistent with the electrochemical deintercalation of Mg²⁺ from MgCr₂O₄. No other mechanisms could be envisaged upon oxidation that would explain these changes, including conversion.⁴ This result is reinforced by recent observations of selective extraction of Mg over Cr from the electrode by operando elemental analysis of the electrolyte in similar conditions,⁴³ which rules out the predominance of corrosion. The XRD pattern of the sample held at 5 V showed minor shifts compared to pristine (Figures 4c and S30), suggesting a slight decrease of the unit cell volume. Intriguingly, a decrease of the ratio of intensity between (111) and (311) reflections was notably visible. Modeling of the changes in diffraction intensity with occupancy of Mg²⁺ in the tetrahedral site of the spinel structure produced the same effect, suggesting that XRD also captured demagnesiation. Unfortunately, the samples were severely damaged upon exposure air or even to laboratory X-rays (Figures 4b, S31, and S32), resulting in the regeneration of the ²⁵Mg MAS NMR signal at ~ 2800 ppm, but at much lower intensity than the pristine state, suggesting chemical degradation. The instability of the charged state to X-ray exposure introduced uncertainty to other possible analyses. The observations are in line with predictions of a substantial instability of the spinel-type Cr₂O₄

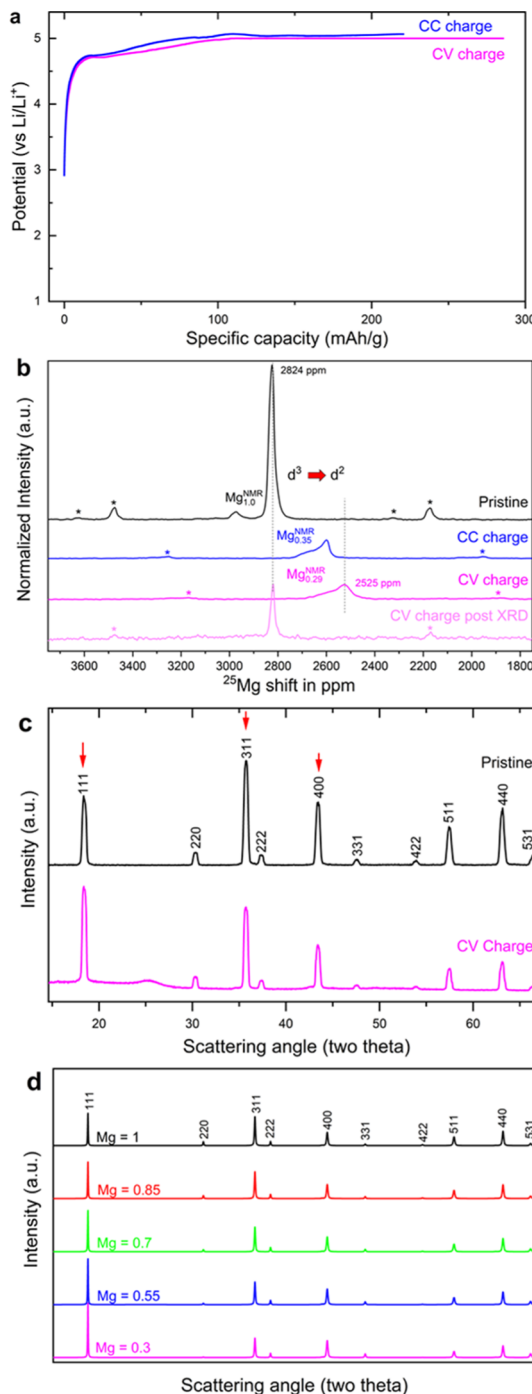


Figure 4. (a) Electrochemical profiles of a cell with MgCr₂O₄ made by sol–gel and a Li metal counter electrode, charged at a constant current to 220 mA h/g and ~ 5 V (CC, C/20) or charged at the same constant current to 5 V, and then held at this constant voltage (CV) for 6 days; both cells contained a Li-ion electrolyte. (b) Quantitative comparison of the ²⁵Mg MAS NMR spectra of pristine and charged samples, collected at 11.7 T; * indicates spinning sidebands. (c) XRD patterns of the electrode in its pristine state and after the CV process; red arrows denote the major changes in intensity. (d) Simulated XRD patterns for Mg_xCr₂O₄, with x indicated in the figure, intended to highlight the changes in relative intensity of the peaks with the content of Mg in the tetrahedral sites. Possible peak shifts were not considered in the simulation.

lattice (rutile CrO₂ being the ground state)⁴² and an apparent limit of about 70% Mg²⁺ that can be removed from the lattice

imposed by Mg-vacancy ordering. Follow-up studies of this complex reaction will be reported elsewhere.

A similar decrease in intensity and shift to lower frequency was observed in the ^{25}Mg MAS NMR of a working electrode of $(\text{Mg})[\text{Mn}]_2\text{O}_4$ charged in Li metal half-cells under similar galvanostatic conditions as sol–gel MgCr_2O_4 (Figure S33), further supporting the existence of suitable diffusion of Mg. In contrast, almost negligible changes were induced in a charged working electrode of $(\text{Mg}_{0.59}\text{Mn}_{0.41})[\text{Mg}_{0.41}\text{Mn}_{1.59}]\text{O}_4$, which remained broad and centered at similar frequencies. This result was also consistent with the increase in hopping barriers with site inversion in the spinel structure, measured both experimentally and computationally.

CONCLUSIONS

Experimental and theoretical techniques revealed that barriers to migration of Mg^{2+} in spinel oxides are within the range postulated to permit Mg battery electrodes. MgCr_2O_4 has a total electrical conductivity of $\sim 10^{-5}$ S/cm at 60°C ,⁴⁴ but subsequent measurements isolating conductivity of Mg^{2+} from electrons were not possible because of the absence of appropriately selective electrodes. Furthermore, highly functional Li-ion battery cathodes have higher electronic than ionic conductivity in their pristine state.⁴⁵ Consistent with the observed migration barriers, electrochemical deintercalation of Mg^{2+} from a bulk normal spinel lattice was possible at acceptable rates, indicating that long-range diffusion exists. The methodology is applicable to study cation dynamics broadly to decouple the role of bulk transport properties of the material from other competing processes in batteries, such as the kinetics of cation desolvation or bulk stability. The high overpotentials and the instability of charged $\text{Mg}_x\text{Cr}_2\text{O}_4$ identify barriers to be addressed. All in all, this study offers renewed impetus in the quest for a practical Mg battery, urging investigations to issues beyond bulk ionic mobility.

ASSOCIATED CONTENT

Supporting Information

The Supporting Information is available free of charge at <https://pubs.acs.org/doi/10.1021/acs.chemmater.9b02450>.

Results of Rietveld refinements; PDF data; additional clarifying plots and explanations of the NMR data presented in the paper; results of fits of the NMR data; raw μSR data and results of the corresponding fits; supplemental DFT calculations; and supplemental EDX, XRD, and NMR measurements of cycled electrodes and their stability (PDF)

AUTHOR INFORMATION

Corresponding Author

*E-mail: jcabana@uic.edu.

ORCID

Baris Key: [0000-0002-1987-1629](https://orcid.org/0000-0002-1987-1629)

Gopalakrishnan Sai Gautam: [0000-0002-1303-0976](https://orcid.org/0000-0002-1303-0976)

Pieremanuele Canepa: [0000-0002-5168-9253](https://orcid.org/0000-0002-5168-9253)

Fulya Dogan: [0000-0001-7997-266X](https://orcid.org/0000-0001-7997-266X)

Peter J. Baker: [0000-0002-2306-2648](https://orcid.org/0000-0002-2306-2648)

John T. Vaughney: [0000-0002-2556-6129](https://orcid.org/0000-0002-2556-6129)

Jordi Cabana: [0000-0002-2353-5986](https://orcid.org/0000-0002-2353-5986)

Author Contributions

^{††}R.D.B. and B.K. contributed equally to this manuscript.

Notes

The authors declare no competing financial interest.

ACKNOWLEDGMENTS

This work was supported as part of the Joint Center for Energy Storage Research (JCESR), an Energy Innovation Hub funded by the US Department of Energy (DOE), Office of Science, Basic Energy Sciences (BES). Use of Advanced Photon Source at Argonne National Laboratory was supported by the US Department of Energy, Office of Science, Office of Basic Energy Sciences, under contract no. DE-AC02-06CH11357. The research performed at Oak Ridge National Laboratory's Spallation Neutron Source was sponsored by the Scientific User Facilities Division, Office of Basic Energy Sciences, US Department of Energy. High-field ss-NMR experiments were performed at the Environmental Molecular Science Laboratory, a national scientific user facility sponsored by the DOE Office of Science, Office of Biological and Environmental Research, and Physical Science Laboratory both located at Pacific Northwest National Laboratory (PNNL). PNNL is a multiprogram national laboratory operated for DOE by Battelle Memorial Institute under contract no. DE-AC05-76RL01830. The authors gratefully acknowledge the UK Science and Technology Facilities Council (STFC) for access to muon beam time at ISIS, and also for the provision of sample preparation under experiment number RB1620415. R.D.B. thanks the Oxford Martin Programme for Integrating Renewable Energy at the Oxford Martin School, University of Oxford, for partial funding. P.C. is grateful to the Ramsay Memorial Trust and University College London for the provision of their Ramsay Fellowship. The authors would like to thank Dr. Katherine Page, Dr. Matthew G. Tucker, Dr. Yuanpeng Zhang, and Dr. Marshall T. McDonnell for assistance in collecting NPD data. They also thank Dr. Niya Sa and Dr. Sang-Don Han for their support in the initial stages of the study. Lastly, the authors are grateful to James C. Knight, Karl T. Mueller, Matthew R. Roberts, Colin Greaves, Peter G. Bruce, and Clare P. Grey for useful discussions.

REFERENCES

- (1) Aurbach, D.; Lu, Z.; Schechter, A.; Gofer, Y.; Gizbar, H.; Turgeman, R.; Cohen, Y.; Moshkovich, M.; Levi, E. Prototype systems for rechargeable magnesium batteries. *Nature* **2000**, *407*, 724–727.
- (2) Muldoon, J.; Bucur, C. B.; Gregory, T. Quest for nonaqueous multivalent secondary batteries: Magnesium and beyond. *Chem. Rev.* **2014**, *114*, 11683–11720.
- (3) Lipson, A. L.; Han, S.-D.; Pan, B.; See, K. A.; Gewirth, A. A.; Liao, C.; Vaughney, J. T.; Ingram, B. J. Practical stability limits of magnesium electrolytes. *J. Electrochem. Soc.* **2016**, *163*, A2253–A2257.
- (4) Canepa, P.; Sai Gautam, G.; Hannah, D. C.; Malik, R.; Liu, M.; Gallagher, K. G.; Persson, K. A.; Ceder, G. Odyssey of multivalent cathode materials: Open questions and future challenges. *Chem. Rev.* **2017**, *117*, 4287–4341.
- (5) Sun, X.; Bonnick, P.; Duffort, V.; Liu, M.; Rong, Z.; Persson, K. A.; Ceder, G.; Nazar, L. F. A high capacity thiospinel cathode for Mg batteries. *Energy Environ. Sci.* **2016**, *9*, 2273–2277.
- (6) Kim, C.; Phillips, P. J.; Key, B.; Yi, T.; Nordlund, D.; Yu, Y.-S.; Bayliss, R. D.; Han, S.-D.; He, M.; Zhang, Z.; Burrell, A. K.; Klie, R. F.; Cabana, J. Direct observation of reversible magnesium ion intercalation into a spinel oxide host. *Adv. Mater.* **2015**, *27*, 3377–3384.

- (7) Gautam, G. S.; Canepa, P.; Richards, W. D.; Malik, R.; Ceder, G. Role of structural H₂O in intercalation electrodes: The case of Mg in nanocrystalline xerogel V₂O₅. *Nano Lett.* **2016**, *16*, 2426–2431.
- (8) Wang, J.; Toby, B. H.; Lee, P. L.; Ribaud, L.; Antao, S. M.; Kurtz, C.; Ramanathan, M.; Von Dreele, R. B.; Beno, M. A. A dedicated powder diffraction beamline at the Advanced Photon Source: Commissioning and early operational results. *Rev. Sci. Instrum.* **2008**, *79*, 085105.
- (9) Lee, P. L.; Shu, D.; Ramanathan, M.; Preissner, C.; Wang, J.; Beno, M. A.; Von Dreele, R. B.; Ribaud, L.; Kurtz, C.; Antao, S. M.; Jiao, X.; Toby, B. H. A twelve-analyzer detector system for high-resolution powder diffraction. *J. Synchrotron Radiat.* **2008**, *15*, 427–432.
- (10) Rietveld, H. M. A profile refinement method for nuclear and magnetic structures. *J. Appl. Crystallogr.* **1969**, *2*, 65–71.
- (11) Neufeld, J.; Feygenson, M.; Carruth, J.; Hoffmann, R.; Chipley, K. K. The Nanoscale Ordered MAterials Diffractometer NOMAD at the Spallation Neutron Source SNS. *Nucl. Instrum. Methods Phys. Res., Sect. B* **2012**, *287*, 68–75.
- (12) Giblin, S. R.; Cottrell, S. P.; King, P. J. C.; Tomlinson, S.; Jago, S. J. S.; Randall, L. J.; Roberts, M. J.; Norris, J.; Howarth, S.; Mutamba, Q. B.; Rhodes, N. J.; Akeroyd, F. A. Optimising a muon spectrometer for measurements at the ISIS pulsed muon source. *Nucl. Instrum. Methods Phys. Res., Sect. A* **2014**, *751*, 70–78.
- (13) Blundell, S. J. Spin-polarized muons in condensed matter physics. *Contemp. Phys.* **1999**, *40*, 175–192.
- (14) Sugiyama, J.; Mukai, K.; Ikeda, Y.; Nozaki, H.; Mansson, M.; Watanabe, I. Li diffusion in Li_xCoO₂ probed by muon-spin spectroscopy. *Phys. Rev. Lett.* **2009**, *103*, 147601.
- (15) Hayano, R. S.; Uemura, Y. J.; Imazato, J.; Nishida, N.; Yamazaki, T.; Kubo, R. Zero-field and low-field spin relaxation studied by positive muons. *Phys. Rev. B: Condens. Matter Mater. Phys.* **1979**, *20*, 850–859.
- (16) Hohenberg, P.; Kohn, W. Inhomogeneous electron gas. *Phys. Rev.* **1964**, *136*, B864–B871.
- (17) Kohn, W.; Sham, L. J. Self-consistent equations including exchange and correlation effects. *Phys. Rev.* **1965**, *140*, A1133–A1138.
- (18) Kresse, G. Ab initio molecular dynamics for liquid metals. *J. Non-Cryst. Solids* **1995**, *192–193*, 222–229.
- (19) Kresse, G.; Furthmüller, J. Efficient iterative schemes for ab initio total-energy calculations using a plane-wave basis set. *Phys. Rev. B: Condens. Matter Mater. Phys.* **1996**, *54*, 11169–11186.
- (20) Perdew, J. P.; Burke, K.; Ernzerhof, M. Generalized gradient approximation made simple. *Phys. Rev. Lett.* **1996**, *77*, 3865–3868.
- (21) Burdett, J. K.; Price, G. D.; Price, S. L. Role of the crystal-field theory in determining the structures of spinels. *J. Am. Chem. Soc.* **1982**, *104*, 92–95.
- (22) Rosenberg, M.; Nicolau, P. Electrical properties and cation migration in MgMn₂O₄. *Phys. Status Solidi B* **1964**, *6*, 101–110.
- (23) Zhang, X.; Zunger, A. Diagrammatic separation of different crystal structures of A₂BX₄ compounds without energy minimization: A pseudopotential orbital radii approach. *Adv. Funct. Mater.* **2010**, *20*, 1944–1952.
- (24) Gautam, G. S.; Canepa, P.; Urban, A.; Bo, S. H.; Ceder, G. Influence of inversion on Mg mobility and electrochemistry in spinels. *Chem. Mater.* **2017**, *29*, 7918–7930.
- (25) Grey, C. P.; Dupré, N. NMR studies of cathode materials for lithium-ion rechargeable batteries. *Chem. Rev.* **2004**, *104*, 4493–4512.
- (26) Lee, J.; Seymour, I. D.; Pell, A. J.; Dutton, S. E.; Grey, C. P. A systematic study of ²⁵Mg NMR in paramagnetic transition metal oxides: applications to Mg-ion battery materials. *Phys. Chem. Chem. Phys.* **2017**, *19*, 613–625.
- (27) Wilkening, M.; Amade, R.; Iwaniak, W.; Heitjans, P. Ultraslow Li diffusion in spinel-type structured Li₄Ti₅O₁₂ - A comparison of results from solid state NMR and impedance spectroscopy. *Phys. Chem. Chem. Phys.* **2007**, *9*, 1239–1246.
- (28) Kuhn, A.; Duppel, V.; Lotsch, B. V. Tetragonal Li₁₀GeP₂S₁₂ and Li₇GePS₈ - exploring the Li ion dynamics in LGPS Li electrolytes. *Energy Environ. Sci.* **2013**, *6*, 3548–3552.
- (29) Cahill, L. S.; Chapman, R. P.; Britten, J. F.; Goward, G. R. ⁷Li NMR and two-dimensional exchange study of lithium dynamics in monoclinic Li₃V₂(PO₄)₃. *J. Phys. Chem. B* **2006**, *110*, 7171–7177.
- (30) Kuhn, A.; Narayanan, S.; Spencer, L.; Goward, G.; Thangadurai, V.; Wilkening, M. Li self-diffusion in garnet-type Li₂La₃Zr₂O₁₂ as probed directly by diffusion-induced ⁷Li spin-lattice relaxation NMR spectroscopy. *Phys. Rev. B: Condens. Matter Mater. Phys.* **2011**, *83*, 094302.
- (31) Fischer, D. M.; Duwe, P.; Indris, S.; Heitjans, P. Tracer diffusion measurements in solid lithium: a test case for the comparison between NMR in static and pulsed magnetic field gradients after upgrading a standard solid state NMR spectrometer. *Solid State Nucl. Magn. Reson.* **2004**, *26*, 74–83.
- (32) Jeon, J.-D.; Kwak, S.-Y. Variable-temperature ⁷Li solid-state NMR investigation of Li-ion mobility and its correlation with conductivity in pore-filling polymer electrolytes for secondary batteries. *Macromolecules* **2006**, *39*, 8027–8034.
- (33) Wong, S.; Zax, D. B. What do NMR linewidths tell us? Dynamics of alkali cations in a PEO-based nanocomposite polymer electrolyte. *Electrochim. Acta* **1997**, *42*, 3513–3518.
- (34) Wang, H.; Senguttuvan, P.; Proffit, D. L.; Pan, B.; Liao, C.; Burrell, A. K.; Vaughey, J. T.; Key, B. Formation of MgO during chemical magnesiation of Mg-ion battery materials. *ECS Electrochem. Lett.* **2015**, *4*, A90–A93.
- (35) Lee, Y. J.; Wang, F.; Grey, C. P. ⁶Li and ⁷Li MAS NMR studies of lithium manganate cathode materials. *J. Am. Chem. Soc.* **1998**, *120*, 12601–12613.
- (36) Waugh, J.; Fedin, E. Determination of hindered-rotation barriers in solids. *Sov. Phys. Solid State* **1963**, *4*, 1633.
- (37) Abragam, A. *The Principles of Nuclear Magnetism*; Clarendon Press, 1982, p 18.
- (38) Bloembergen, N.; Purcell, E. M.; Pound, R. V. Relaxation effects in nuclear magnetic resonance absorption. *Phys. Rev.* **1948**, *73*, 679–712.
- (39) Baker, P. J.; Franke, I.; Pratt, F. L.; Lancaster, T.; Prabhakaran, D.; Hayes, W.; Blundell, S. J. Probing magnetic order in LiMPO₄ (M = Ni, Co, Fe) and lithium diffusion in Li_xFePO₄. *Phys. Rev. B: Condens. Matter Mater. Phys.* **2011**, *84*, 174403.
- (40) Liu, M.; Rong, Z.; Malik, R.; Canepa, P.; Jain, A.; Ceder, G.; Persson, K. A. Spinel compounds as multivalent battery cathodes: a systematic evaluation based on ab initio calculations. *Energy Environ. Sci.* **2015**, *8*, 964–974.
- (41) Rong, Z.; Malik, R.; Canepa, P.; Sai Gautam, G.; Liu, M.; Jain, A.; Persson, K.; Ceder, G. Materials design rules for multivalent ion mobility in intercalation structures. *Chem. Mater.* **2015**, *27*, 6016–6021.
- (42) Chen, T.; Sai Gautam, G.; Huang, W.; Ceder, G. First-principles study of the voltage profile and mobility of Mg intercalation in a chromium oxide spinel. *Chem. Mater.* **2018**, *30*, 153–162.
- (43) Lopes, P. P.; Zorko, M.; Hawthorne, K. L.; Connell, J. G.; Ingram, B. J.; Strmcnik, D.; Stamenkovic, V. R.; Markovic, N. M. Real-time monitoring of cation dissolution/deintercalation kinetics from transition-metal oxides in organic environments. *J. Phys. Chem. Lett.* **2018**, *9*, 4935–4940.
- (44) Stefan, E.; Irvine, J. T. S. Synthesis and characterization of chromium spinels as potential electrode support materials for intermediate temperature solid oxide fuel cells. *J. Mater. Sci.* **2011**, *46*, 7191–7197.
- (45) Amin, R.; Ravnsbæk, D. B.; Chiang, Y.-M. Characterization of electronic and ionic transport in Li_{1-x}Ni_{0.8}Co_{0.15}Al_{0.05}O₂ (NCA). *J. Electrochem. Soc.* **2015**, *162*, A1163–A1169.